Assessment of the effect of embedded RFID tag on a composite laminate strength

Ambrosini, Daniele; Zarouchas, Dimitrios; Pirondi, Alessandro; Vescovi, Luca

DOI
10.1016/j.compscitech.2024.110691

Publication date
2024

Document Version
Final published version

Published in
Composites Science and Technology

Composites Science and Technology 255 (2024) 110691

Contents lists available at ScienceDirect

Composites Science and Technology

journal homepage: www.elsevier.com/locate/compscitech

Assessment of the effect of embedded RFID tag on a composite laminate strength

Daniele Ambrosini [d], Dimitrios Zarouchas [b], Alessandro Pirondi [a,*], Luca Vescovi [c]

[a] Department of Engineering for Industrial Systems and Technologies, University of Parma, Parma, Italy
[b] Delft University of Technology, Delft, Netherlands
[c] Dallara Automobili S.p.A., Varano De'Melegari, Italy
[d] Department of Industrial Engineering, University of Bologna, Bologna, Italy

ARTICLE INFO

Keywords:
RFID
Composite laminates
Damage
C-scan
Acoustic emission
DIC

ABSTRACT

RFID (Radio Frequency Identification) is commonly used to monitor goods along the supply chain. The feasibility of the application of a RFID tag to monitor CFRP components was demonstrated in a previous work by some of the authors. This work is aimed at evaluating how the integration of a RFID tag inside a CFRP laminate affects the quasi-static strength and the failure mode. Finite element modelling is used to design a specimen with an embedded tag, that may be representative of the tensile state of stress in a larger laminate. Tensile testing is performed both up to failure and by interrupting tests at different load levels in order to inspect the specimen by C-scan. Acoustic Emission (AE) and Digital Image Correlation (DIC) are used as additional non-destructive monitoring techniques. Some interrupted tests were selected to extract micrographic sections that illustrate damage development in the laminate. The extensive destructive and non-destructive characterization allowed to quantify the effect of embedding a RFID tag in the laminate in terms of strength decrease and failure mode.

1. Introduction

The increase in data and information generated by industrial production has turned into a series of opportunities to improve many industrial applications by connecting machinery, objects and personnel to a central control system without the use of wires, also referred to as Industry 4.0 paradigm [1].

One technology that has a significant impact in this context is RFID (Radio Frequency IDentification). Today, with recent discoveries and new protocols, it is possible to enable sensing capabilities [2] to the primary function of tracking and identification [3,4]. The application of RFID can be associated with a variety of fields, from supply chain and logistics to the healthcare industry, to automotive and aerospace [5]. The main characteristics associated to RFID is to have a unique ID (UID, 96 bits typically) associated with an object, which ensures a precise traceability in- and outside the factory, because of the possibility of reading without human intervention; besides, it increases the difficulty of counterfeiting.

The RFID technology is based on three elements: the tag, the interrogator and a host computer. The RFID tag comprises a chip and an antenna, and it is chosen according to the application field. The interrogator, consisting of an antenna and a reader, radiates and receives the elctromagnetic (EM) signal to and from the RFID tags. Recently, UHF (Ultra-High Frequency) tags were developed in order to be mounted on a metal surface. In this way, this latter is exploited as an expanded antenna and therefore the tag size can be reduced; for this reason they are called on-metal tags. The chip and and the antenna of an on-metal tag are embedded in a rigid enclosure that makes the tag resistant to high temperatures and/or pressures, and even to aggressive chemicals. This type of RFID tag can therefore resist to the cure cycle of laminated composite materials, allowing for the embedding inside the component instead of attaching it externally. In this way, the tag is protected from the environment during the service life of the component and it ensures a better countefeiting action since it is much less visible.

The use of RFID systems to optimise the process along the production chain is growing in the automotive industry [5,6] and composite materials manufacturers involved in the value chain have therefore started to move in this direction. In Refs. [7,8] the authors placed a RFID tag on a CFRP (Carbon Fiber-Reinforced Polymer) base, paying attention to the positioning process and to the material and shape of the tag cover, since

* Corresponding author. University of Parma, Department of Engineering for Industrial Systems and Technologies, Parco Area delle Scienze 181/A, 43124, Parma, Italy.
E-mail address: alessandro.pirondi@unipr.it (A. Pirondi).

https://doi.org/10.1016/j.compscitech.2024.110691
Received 18 October 2023; Received in revised form 28 March 2024; Accepted 29 May 2024
Available online 31 May 2024

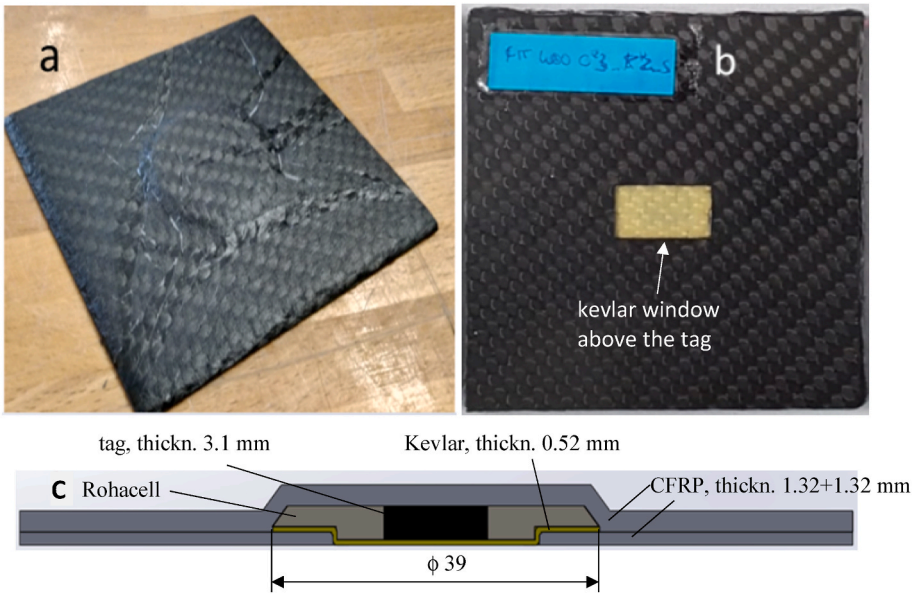

Fig. 1. Cured CFRP coupon with embedded tag: a) backside; b) front side; c) transverse section.

carbon fibers are conductive and, therefore, tend to shield the electromagnetic waves. Gorski et al. [9] applied a RFID tag to a linen and carbon fiber component and evaluated the signal attenuation/amplification of several UHF tag on different composite materials. In Ref. [10], a preliminary study was evaluated by placing a UHF tag on conductive surfaces such as CFRPs and steel. In a previous work [11], some of the authors identified a configuration for embedding the tag inside a CFRP laminate, while keeping at the same time a good reading distance, placing an on-metal tag in a groove inside the laminate and leaving a window in the CFRP plies to let the electromagnetic signal propagate outside. In order to hide the tag from the exterior, the window was closed using glass fiber plies, that are trasparent to EM waves. The tag chosen was Fit 400 HT from Omnia, Gurugram, India, having a 13.1 x 7.8 × 3.1 mm^3 size. That configuration (see Fig. 1) was tested for reading distance after curing in Ref. [12], confirming the results obtained in Ref. [11].

The literature survey demonstrates that the number of studies on the use of RFID tags with CFRP materials is very limited, and just the authors of the present paper assessed the readibility of the tag inside a CFRP laminate after curing, [12]. However, the embedding in the laminate produces a prominent bulge, with a thickness equal to the one of the tag and an inner diameter of 39 mm, see Fig. 1. The Kevlar window and the bulge shown in Fig. 1 have to lie on opposite sides of a component. Namely, the window has to be on the external side (front side) to allow for reading the tag and the bulge on the inner side (back side) for aesthetics and aerodynamic motivations and also to avoid the identification of the tag location when used for counterfeiting purpose. Aesthetics and counterfeiting of course require that, when the tag is embedded into a real component, the Kevlar window has to be someway hidden, such as black painted, or else.

Looking at the cross-section drawn in Fig. 1, it is evident that the presence of the tag generates several weakening points in the CFRP laminate:

- stress concentration at the corners of the opening in the CFRP on one side of the laminate;
- complex interface shape between the CFRP and Kevlar, which may be prone to delamination;
- presence of the Rohacell insert that gives raise to a large bulge in the laminate, a source of stress concentration and potential delamination problems in the CFRP;
- formation of resin pockets between CFRP plies along the perimeter of the bulge, and between Kevlar and CFRP along the perimeter of the opening in the CFRP, where cracks may easily develop.

Tougher, nacre-like structures might be adopted for the composite laminate [13], and also graphene –wrapped B_4C nanowires [14] or nanoclays [15] have demonstrated to reinforce composite interfaces. However, the potential for intra- and interlaminare failure in bulge region would still exist, and no attempt to evaluate how the tag inside a CFRP laminate affects the quasi-static strength and the failure mode was found yet in the literature.

The novelty of this work relies therefore in two main points:

1. the identification of the impact on the safety margin of a CFRP laminate in real-world applications, in order to let the designer take the appropriate counteracting measures;
2. the identification and the classification of the failure mechanisms acting under quasi-static loading. This paves the way for numerical modelling of failure as well as it is helpful to address fatigue testing.

A set of numerical as well as experimental techniques are deployed for such purposes:

- finite element modelling (FEM) is used to design a specimen with an embedded tag, that may be representative of the tensile state of stress in a larger laminate;
- tensile testing is performed both up to failure and by interrupting tests at different load levels in order to inspect the specimen by C-scan;
- C-scan is used to reveal the progression of failure, espcially in terms of delamination, from interrupted tensile tests;
- Acoustic Emission (AE) and Digital Image Correlation (DIC) are used as additional non-destructive monitoring techniques in order to possibly discriminate the failure mechanisms acting in the laminate under tensile test;
- some interrupted test were selected to extract micrographic sections that illustrate damage development in the laminate.

The extensive destructive and non-destructive characterization allowed to quantify the effect of embedding a RFID tag in the laminate in terms of strength decrease and failure mode. The strength of the

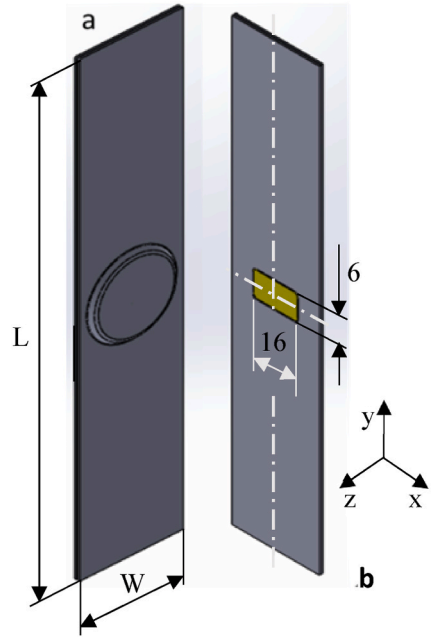

Fig. 2. Tensile test specimen: a) back side; b) front side. Load is applied in direction y.

methodology is that it can be used in any case where the effects on strength of a tag embedded into a composite laminate, not necessarily carbon-reinforced, have to be assessed to support the design. The use of FEM here is intentionally limited to the design of the specimen for testing, since an experimental approach has been preferred for the identification of damage development: the knowledge of real mechanisms first, will facilitate the build-up of an effective numerical model of failure in future. On the other hand, this work is limited to uniaxial, quasi-static loading, thereby leaving the field open about biaxial/multiaxial and fatigue loading conditions.

2. Methodology

2.1. Design of Tensile test samples

The objective of this section is to identify a specimen for tensile testing containing a local bulge caused by the presence of the tag. Since the stress concentration caused by the bulge is dependent on the size of the specimen with respect to the size of the bulge, various specimen dimensions were simulated, looking for the minimum one that ensures the same stress distribution of larger sizes.

The study was done by Finite Element Analysis (FEA) using the software Abaqus 2017® from Dassault Systèmes. The specimen shape is shown in Fig. 2, where the bulge caused by the RFID tag is also visible. The baseline size is L = 250 mm, W = 50 mm. Nine different models have been then generated by scaling up L and W and combining them. The scale factor is 1, 1.5 and 2 times the baseline values, respectively. All the other sizes are kept constant, as given in Figs. 1c and 2b, since these values come from the study performed in Ref. [12]. The Kevlar window (in yellow in Fig. 2) has been placed with the major axis transverse to the applied force, in order to reduce as much as possible the net section of the CFRP front plies (worst-case scenario). Oblique orientations have not been considered in this first assessment. One quarter of the entire model was modelled thanks to symmetry.

The layup and the lamination process also come from Ref. [12] and it is a representative figure of structural composite skins manufactured by Dallara srl, Varano Melegari, Italy. The CFRP is GG 630 T700 12K 2x2 DT120 37 % (Deltapreg, Teramo, Italy) with a ply thickness of 0.66 mm. The Kevlar insert is made of AA285 170 DT 120 50 % (Deltapreg, Teramo, Italy) with a ply thickness of 0.26 mm and the polymeric foam surrounding the tag is Rohacell 71 WF (Evonik Industries AG, Essen, Germany). The mechanical properties from supplier datasheets are summarized in Table 1.

Table 1
Mechanical properties of the CFRP and Kevlar plies and of Rohacell. For the two composite materials, tensile strength is taken equal in the longitudinal (1) and transverse (2) directions.

Material	Tensile Modulus [MPa]		Shear Modulus [MPa]	Poisson Ratio [−]	Tensile Strength [MPa]
	E_1	E_2	G_{12}	ν_{12}, ν	X_T, σ_u
GG 630 T700	58500	58150	5000	0.03	900
AA 285 170	27500	29900	1900	0.08	476
Rohacell 71 WF	105		42	0.25	2.2

In order to make a better discretization of the FE model, the specimen domain was subdivided into four main parts, connected to each other by rigid kinematic coupling. The four parts are shown in Fig. 3, and correspond to:

a) two plies of CFRP with the "window" to let the electromagnetic signal reach the tag, that correspond to the front side of the specimen;
b) two Kevlar plies shaped to conform the insert to the CFRP window;
c) the Rohacell insert with the cavity for the tag. This latter is not modelled since it is assumed as not structurally collaborating;
d-e) two plies of CFRPs, modelled separately for meshing reasons, that correspond to the back side of the specimen

All plies were oriented at 0° with respect to axis 1 in Fig. 3. Additional volumes, not shown here, were defined to simulate the resin pockets formed at the drop-off between CFRP and Kevlar plies.

The composite parts were meshed with 8-node Continuum Shell, Reduced integration elements with hourglass control (SC8R). On the other hand, 8-node linear bricks (C3D8) were assigned to the Rohacell insert and the neat resin parts were discretized with 4-node linear tetrahedrons (C3D4). The mesh size was set after a convergence analysis on stresses, on the baseline size; the element size was then kept constant in the bulge region for all the configurations, while further elements were added in order to mesh larger sizes. Boundary conditions and loads were set as follows in order to reproduce a tensile test:

- symmetry conditions with respect to X and Y in Fig. 3awere set on the two symmetry planes of the specimen;
- a node on the upper edge in Fig. 3awas restrained in Z-direction to prevent translation in that direction;
- a constant stress equal to 100 MPa was applied at the specimen free end.

The highest value of the Failures Index (FI, Tsai-Hill criterion) in the CFRP, where the final failure occurs, occurs in the window corner on the front side and it is reported in Table 2. It is evident that the various configurations are quite close to each other with respect to the FI (see Table 3).

The stress distribution is similar in all cases (the same FI can be obtained in principle with different stress distributions), too (see Fig. 4). The three tensile components in the principal material directions, σ_{11}, σ_{22} and σ_{33}, are shown qualitatively (red = tensile, blue = compressive) for the baseline size in Fig. 5a–f as an example. The detail is given in Table 4 for the various specimen sizes; the points where the maximum stress values are extracted are the same for all the configurations.

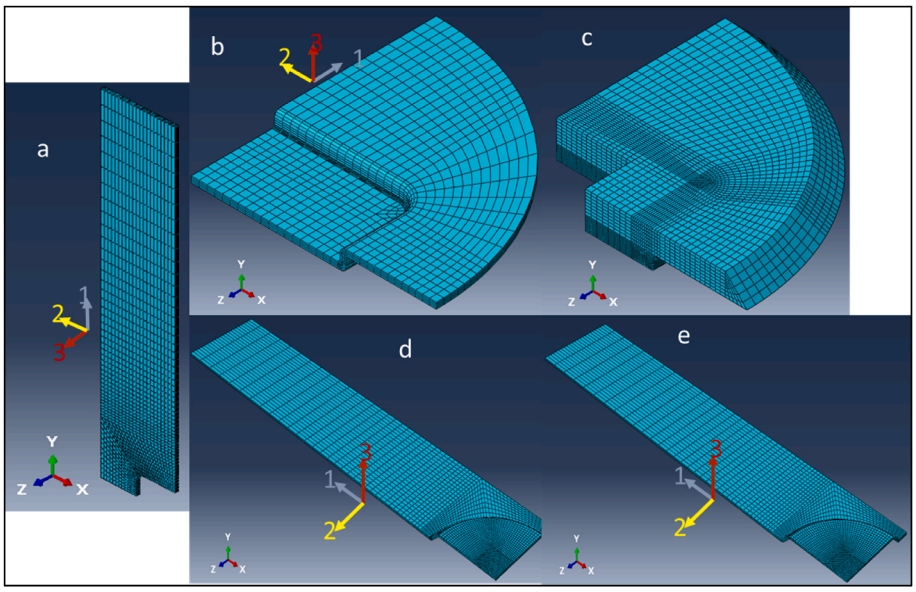

Fig. 3. Meshed parts of the model in Abaqus: a) front CFRP plies; b) kevlar; c) Rohacell; d-e) back CFRP plies.

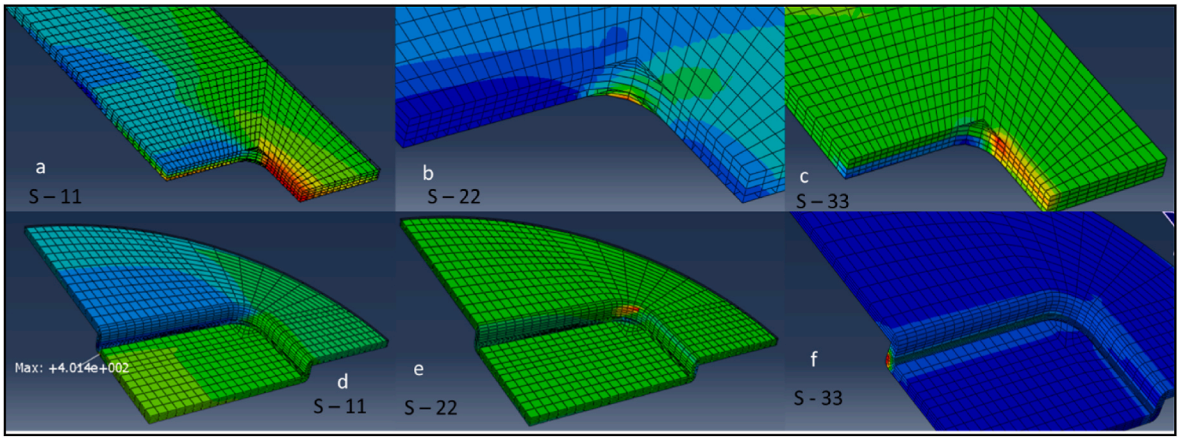

Fig. 4. Stress tensile test simulation a) S11, b) S22, c) S33 in the CFRP, d) S11, e) S22, f) S33 in the Kevlar insert.

Table 2
Highest value of Failure Index (Tsai-Hill criterion) in the CFRP. Baseline (1x) is L = 250 mm, W = 50 mm.

		L		
	Specimen size	1x	1.5x	2x
W	1x	0.66	0.66	0.67
	1.5x	0.66	0.69	0.7
	2x	0.69	0.68	0.62

It is possible to note that the stresses vary from size to size in a narrow range encompassing the baseline (L = 250 mm, W = 50 mm). This means the latter is already large enough to yield, from the engineering standpoint, a steady stress distribution with respect to larger values of L and W. The specimens were therefore manufactured with the baseline size.

2.2. Specimen manufacturing and tensile test

The specimens were manufactured by a cure cycle in an autoclave at 120 °C at 2 bar for 120 min. The first part to be cured is composed by the two Kevlar plies and the Rohacell; HexBond™ ST1035, a 150 gsm supported epoxy adhesive film supplied by Hexcel (Stamford, USA) is placed between Kevlar and Rohacell before curing. The two CFRP plies on the front side of the specimen are then cut to create a rectangular window where the Kevlar + Rohacell cured insert is placed with the interposition of HexBond™ ST1035 film between CFRP and Kevlar. Co-bonding of the insert and the CFRP ends by placing a further layer of HexBond™ ST1035 over the Rohacell, laying down two CFRP plies to form the back side of the specimen, wrapping all in a vacuum bag and applying the cure cycle. A plate containing 9 specimens was created with this procedure, that was then waterjet cut. Tabs were secondary bonded at the specimen ends in order to ensure proper gripping into the testing machine. The specimen is shown in Fig. 5 without tabs.

The testing machine is an electromechanical MTS (MTS Systems Corp., Eden Prairie, USA) equipped with a 100 kN load cell. Tests were performed to failure (five repetitions) or up to interruption at a prescribed load (three repetitions). Concerning interrupted tests, the procedure included testing until the first load level, unloading, unmounting the sample from the testing machine, performing C-scan, reinstall the specimen with AE and DIC instrumentation, run until the next load level and so forth until failure. Five load levels were defined where to stop testing, namely 11, 22, 33, 44 and 50 kN.

The test speed of 1 mm/min was set so that the Acoustic emission

Table 3
Stress simulated in FEM analysis (in MPa).

Size	CFRP						Kevlar					
	σ_{11}	σ_{22}	σ_{33}	σ_{12}	σ_{13}	σ_{23}	σ_{11}	σ_{22}	σ_{33}	σ_{12}	σ_{13}	σ_{23}
L x W	262	94	30	46	32	14	400	140	92	27	16	16
L x 1.5W	264	79	30	46	36	10	349	133	96	29	8	13
L x 2W	275	87	32	46	36	12	404	142	89	26	8	16
1.5L x W	265	89	30	45	35	12	329	140	83	27	7	13
1.5L x 1.5W	260	79	29	46	35	18	378	133	87	26	8	13
1.5L x 2W	272	94	29	49	35	17	380	138	84	24	7	15
2L x W	279	85	28	48	35	22	375	138	83	24	14	15
2L x 1.5W	279	90	28	47	35	22	373	137	83	24	14	15
2L x 2W	246	94	28	43	35	16	372	133	86	26	14	14

L = 250 mm; W = 50 mm.

Fig. 5. Image of tensile composite specimens a) front and, b) back.

Table 4
Acoustic emission acquisition parameters.

Parameters	Value
Sampling rate for the acquisition of AE features	10 MHz
Sampling rate for the acquisition of AE transient waveforms	2 MHz
Amplitude threshold	55 dB
Rearm time	200 μs
Cut-off-frequency (minimum frequency of acquisition)	25 kHz
Duration discrimination time (time window to register each AE signal)	200 μs
Digital pass-band filter	25 kHz–850kHZ

(AE) system could not hear too much noise while acquiring data. The force and displacement of the machine crosshead were recorded throughout the test. The test data acquisition includes also Digital Image Correlation (DIC) and AE. DIC includes two cameras on the front and one on the side of the specimen. The outline of the test setup is shown in Fig. 6.

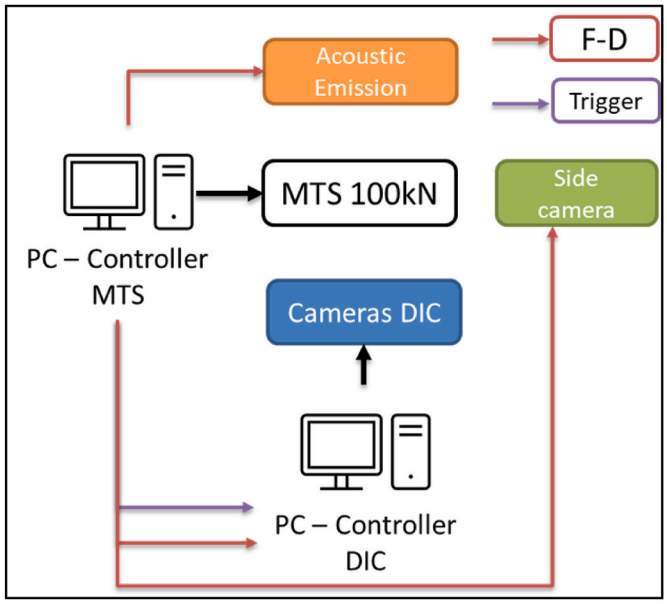

Fig. 6. Test setup.

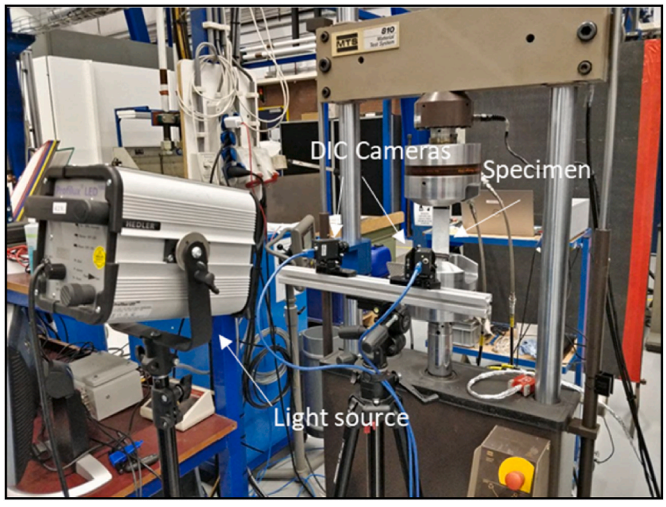

Fig. 7. DIC setup.

2.3. DIC equipment

The VIC-3D system (Correlated Solutions, Inc., Irmo, USA) was used for both image acquisition and post-processing to estimate the

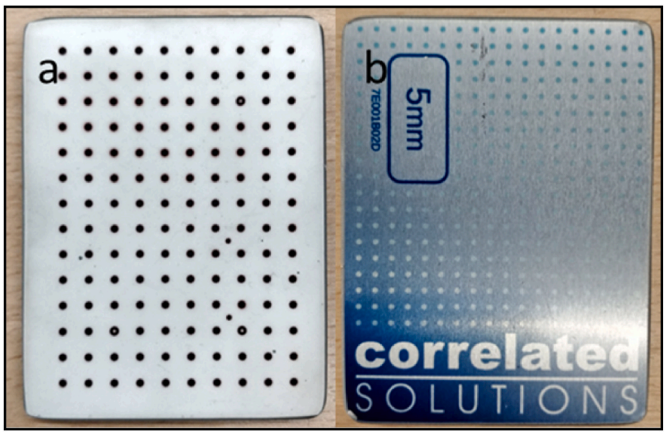

Fig. 8. Calibration panel a) front, b) back.

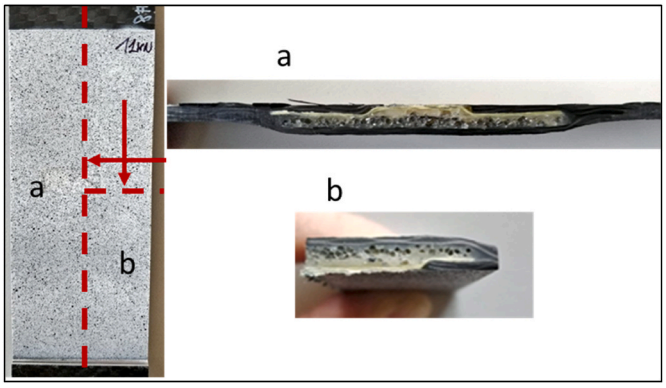

Fig. 9. Example of the sample tested at 11 kN, a) longitudinal section, b) cross-section.

deformation field. The DIC measurement system consist of two 9 Mp resolution cameras, with 25 mm lenses and stereo-angle equal to 30°. The side camera is an Optomotive Velociraptor with a 2.2 MP resolution and a 50 mm lens The cameras were connected to the VIC Gauge acquisition system. Each frame acquired by VIC-3D was synchronised for with the corresponding load and displacement values. The sampling frequency of the acquired images is 2s. A fine speckle pattern was prepared on the front side of five specimens by distributing a thin layer of white non-glossy spray paint first and, afterwards a black non-glossy paint was sprayed onto it. The speckle pattern size obtained in this way is 6.93 pixels, corresponding to 0.378 mm. Tensile test with DIC were run without interruptions. A picture of the test setup is given in Fig. 7. The working distance is 572 mm.

The calibration of the DIC-3D system process was carried out by placing the mask shown in Fig. 8 in the plane where the specimen is positioned for testing and taking images at different positions and rotations of the mask to setup correlation parameters. Light was balanced in order to minimize reflexion spots.

Other parameters of the DIC setup are:

- subset size: 29 pixels;
- step size: 7 pixels
- displacement accuracy (standard deviation confidence in the match): 0.0126 pixels

2.4. C-scan equipment

Interrupted tensile tests were examined using C-scan by removing the sample from the testing machine and placing it in a water-filled tank

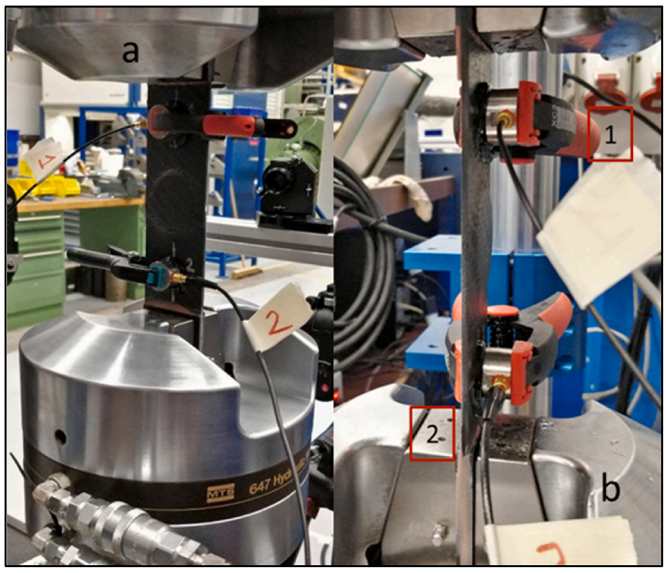

Fig. 10. Acoustic emission sensors positioned during the Tensile tests a) back view b) side view.

before and after testing. The system is an Olympus EPOCH 650.

2.5. Optical microscopy (OM)

Micrographs were taken under an optical microscope to describe the internal damage of the sample. Three specimens were loaded up to 33, 44, 50 kN and to failure, respectively and then cut longitudinally and transversely as described in Fig. 9. The sectioned parts were polished before OM examination. The images were acquired with a Leica DMi8 M/C/A inverted light microscope (Leica Microsystems srl, Milan, Italy).

2.6. AE equipment

The AE measurement setup (Vallen Systeme GmbH, Wolfratshausen, Germany) is shown in Fig. 10. The system is composed of the two VS900-M PZT sensors working in the frequency range 100–900 kHz; each sensor is connected to a 34 dB AEP5 pre-amplifier and connected in turn to a four-channel ASMY-6 acquisition unit through low-noise cables. AE events acquisition was managed by Vallen AE-Suite Software R2020.1124.2.

The two AE sensors were positioned 100 mm apart. A pencil-lead break test was performed to verify the transducer coupling, as recommended by the ASTM E750 standard. The acquisition parameters, set after preliminary tuning, are summarized in Table 4.

2.7. AE data analysis

AE events and their waveforms can give us important information about the type of damage involved in the material, such as matrix cracking, fibre-matrix debonding, fibre breakage, fibre pull-out or delamination and debonding [16]. AE events associated with matrix cracking are characterized by medium-high amplitudes and low frequencies [17], but it can associate also to a low amplitude and low frequency [18,19]. The amplitude emitted by fibre pull-out varies greatly depending on the material used and on the test. The amplitude range is between 70 and 100 dB [20] and with frequencies around 180 kHz [21] and 300 kHz [22]. Some authors suggest that the signal obtained from damage due to delamination has generally a high duration [22,23] with high amplitude signals [17]. As far as fibre breakage is concerned, a high energy release with high amplitudes and a fast rise-time of the waveform is expected from this phenomenon [24].

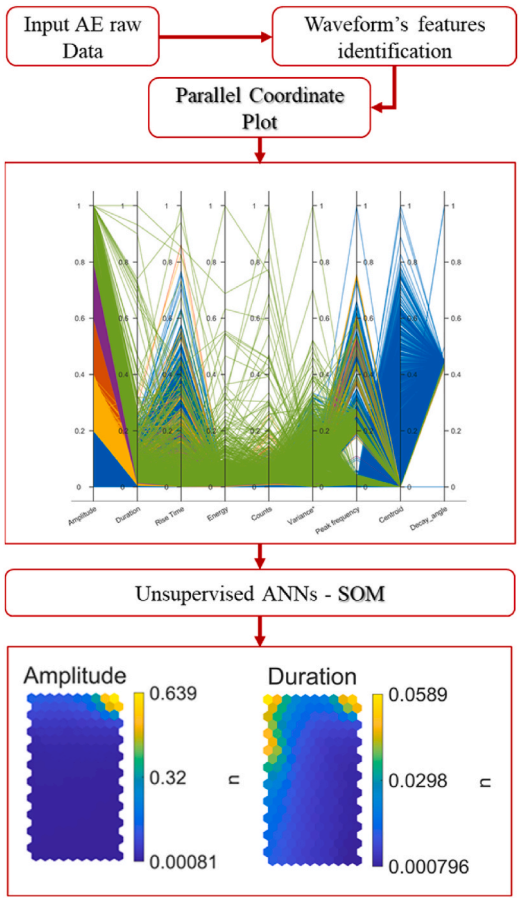

Fig. 11. AE data analysis procedure (ANN = Artificial Neural Network; SOM = Self Organizing Map).

Besides, there are mainly two types of AE signals: continuous and transient ("bursts"). The former is usually produced by external friction or friction within the structure and it is not generally correlated to material damage. Therefore, a filtering of AE bursts from the background continuous noise was done setting a threshold signal by preliminary experiments. The time the signal exceeds the threshold is called the "arrival time" of the burst and is crucial to timely locate the event. A signal that exceeds the threshold is called hit.

An AE data analysis procedure has been therefore defined and the workflow is represented in Fig. 11. Based on the amplitude ranges and the literature, it is possible to associate each cluster with a damage type. Clusters with higher and time-increasing energy levels, where waveforms are of the burst type, are generally associated to damage. On the other hand, background noise produces waves with lower energy levels that are fairly constant over time.

In the feature identification step, the following features of the signal were extracted:

- Amplitude, in dB,
- Duration in μs,
- Energy in eu (1 eu = 10^{-14} V^2s),
- Counts: the number of oscillations of the waveform,
- Rise-Time in μs,
- Decay Angle (in μs),
- Variance (the amplitude variability of the acoustic emission signals)
- Frequency of the centroid: helpful to characterize the overall frequency content of an acoustic emission signal.

The Parallel Coordinate Plot (PCP) has been applied here, alike [25], to understand the correlation between features (normalised values from 0 to 1 are used for the representation). Each line corresponds to a single value of the AE event dataset and describes the relationship existing between the two parameters (axes) it connects. In the PCP plot, lines of different colour represent the different segments into which to [0, 1] interval of normalised values is divided (in Fig. 11 intervals are defined based on the Amplitude feature). The colouring allows to understand better whether there are or not overlaps between the lines and how they are distributed. If the lines between two vertical axes are parallel, there is a strong and positive correlation among the corresponding features; if there is a disordered overlap between the lines, there is no correlation. Finally, if the lines converge at one point without excessively overlapping, there is a strong negative (inverse) correlation. For example, as shown in Fig. 11, the parameters with a more defined correlation are *amplitude* and *duration*.

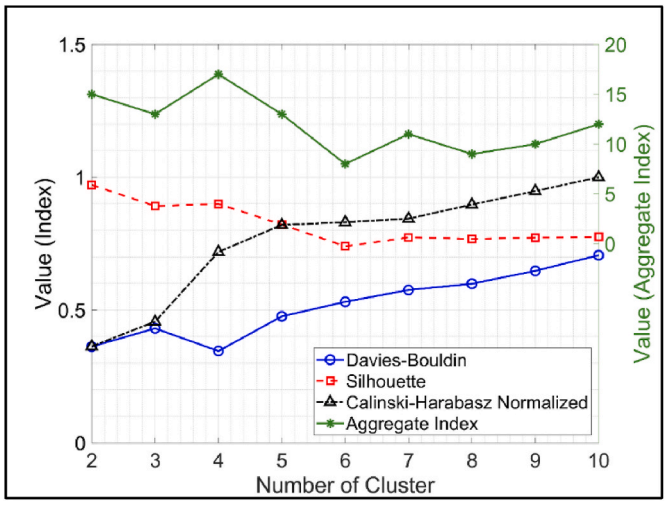

Fig. 12. Index values for each criterion (Value - Index) and aggregate index value to predict the optimal cluster.

Amplitude and *duration* parameters are given in input to the ANN-SOM algorithm that groups them into a certain number of clusters. The procedure for the evaluation of the optimal number of clusters, was based on the use of three indexing criteria, as described by Crivelli et al. [26]:

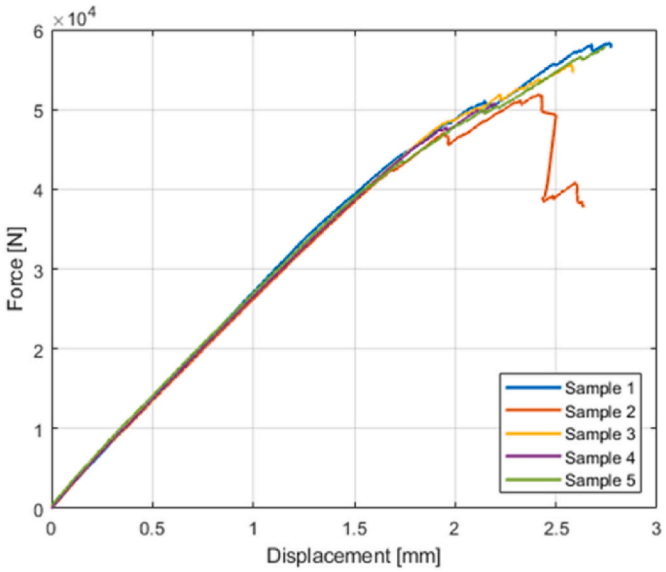

Fig. 13. Force vs Displacement data.

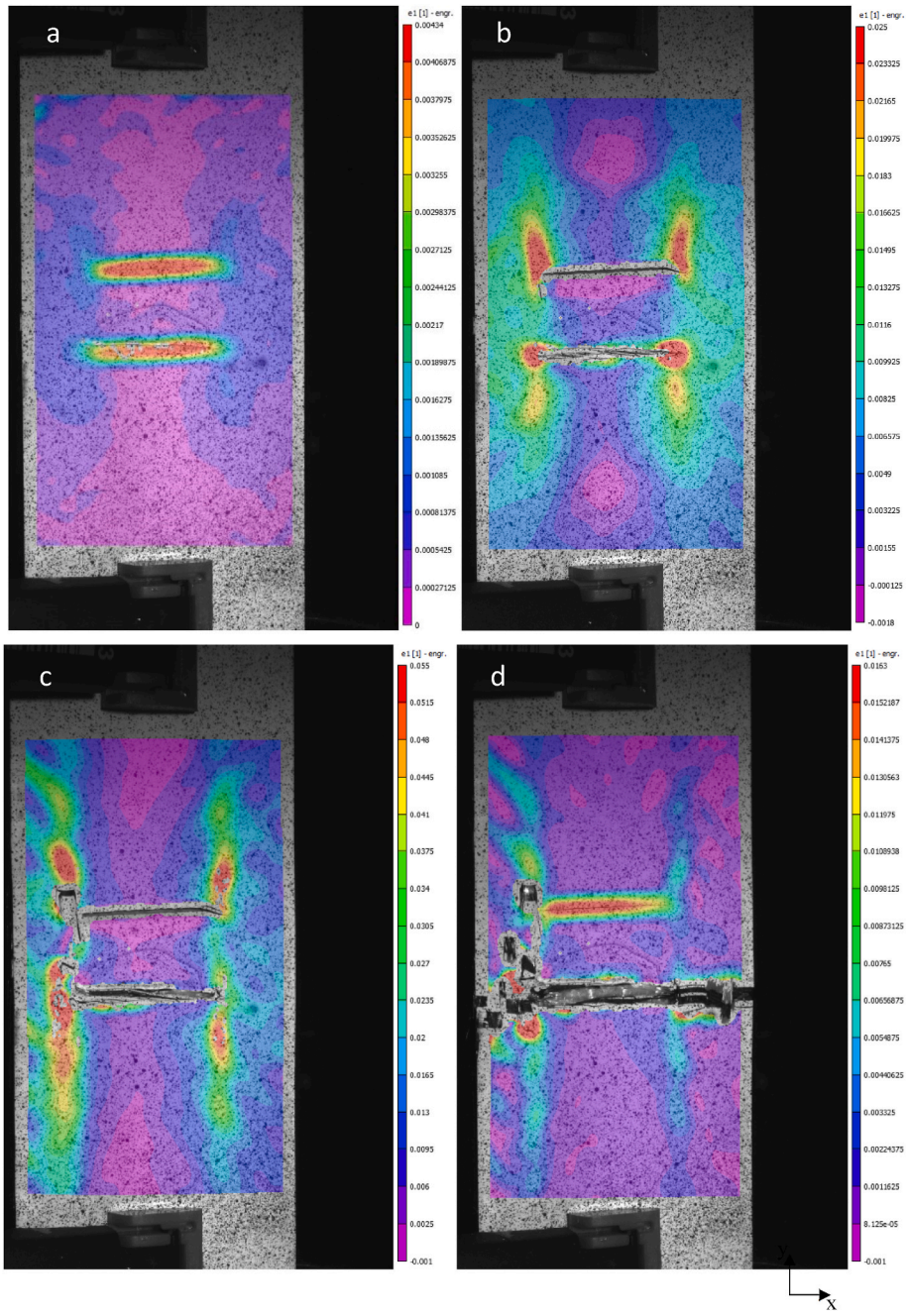

Fig. 14. DIC longitudinal strain field (ε_{yy}) at force levels: a) 15 kN, b)36 kN, c) 58 kN, d) after failure.

1. Silhouette [27].
2. Davies-Bouldin [28].
3. Calinski-Harabasz [29].

The minimum and the maximum number of clusters considered are 2 (c_{min}) and 10 (c_{max}), respectively. The identification of the optimal number of clusters is done based on the maximum aggregate index value (Fig. 12). In the case shown in Fig. 12 the optimal number of clusters is four.

The process described previously was performed for each specimen examined. The classification provided similar results on different specimens and identified an optimal clustering of data using four clusters. Therefore, AE features were clustered using the ANN-SOM algorithm and four clusters for all the experiments.

3. Results and discussion

3.1. Tensile test

Fig. 13 shows the force-displacement curves obtained with individual specimens until failure. It can be seen that all specimens behave similarly in the elastic region, while partial drops of the force start above 40 kN, that may indicate delamination. The average force at failure is 54.89 kN with a standard deviation of 3.43 kN. Being the tensile strength of the CFRP equal to 900 MPa (see Table 1), a bulk CFRP, plain specimen having the same width (50 mm) and thickness (2.5 mm) of the one under test, should exhibit a failure load of 112.5 kN. Therefore, the presence of the tag and related geometrical and material features cause a reduction in strength of a factor of 2.05 in average.

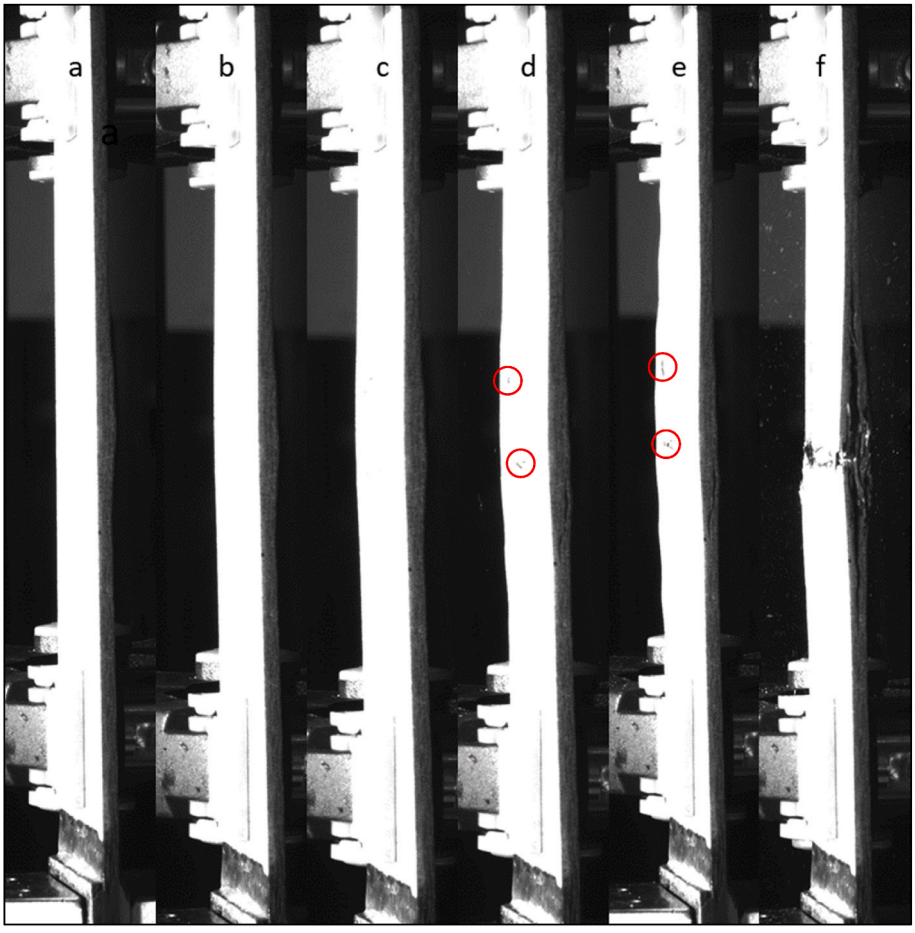

Fig. 15. Photo of the side of the sample at force levels: a) 0 kN, b)15 kN, c)36 kN, d)50 kN, e)58 kN, d) after failure. Red circle indicate the appearance of cracks on the side.

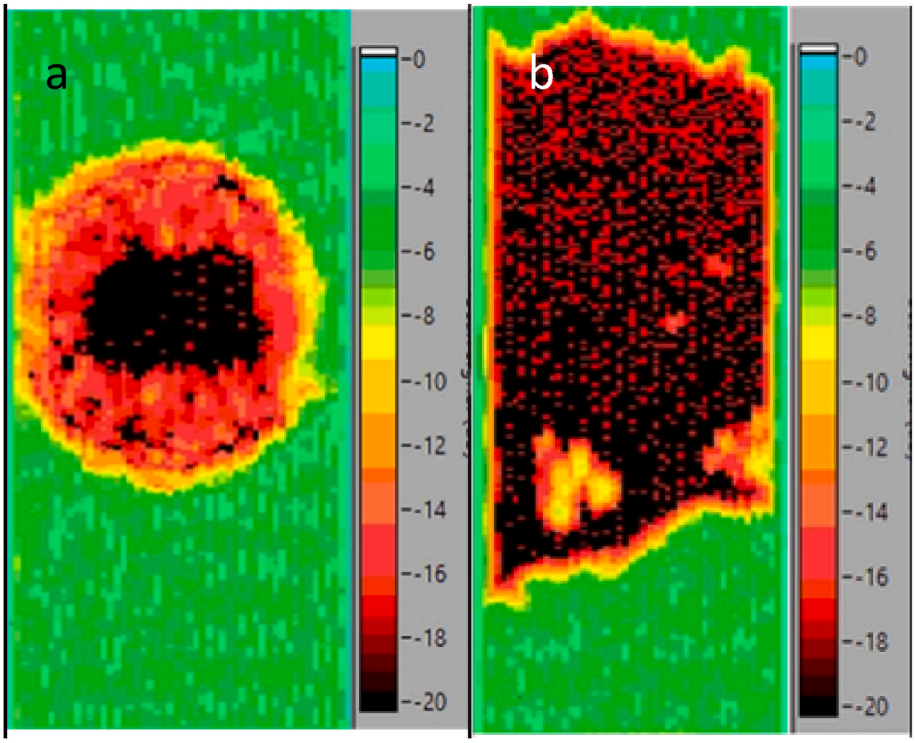

Fig. 16. C-scan contour map: a) at the beginning of the test; b) after failure. The scale represents the attenuation of ultrasound wave in dB.

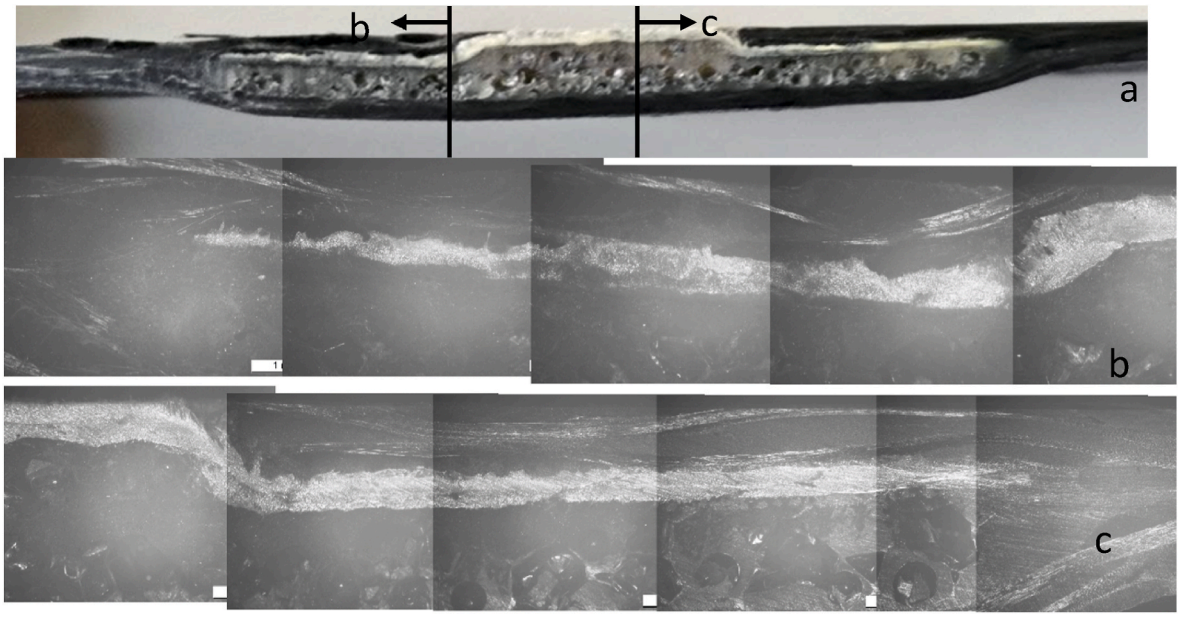

Fig. 17. a) longitudinal section, b) magnification of left side, c) magnification of right side at 33 kN load.

3.2. DIC analysis

The strain field obtained from the analysis of the images taken with the DIC is shown in Fig. 14, illustrating the evolution of the longitudinal strain distribution on the front side of the specimen during the test. At low loads, around 25 % of the failure one, a local strain concentration arises at the carbon/kevlar (C/K) interface (Fig. 14a). Further increase in load causes transverse cracking and subsequent debonding of the C/K interface. From this point onwards, the load is completely transferred to the carbon at the sides of the kevlar insert. As the test continues, the strain concentration increases to the corners of the C/K interface (Fig. 14b).

In the last stages of the test, noticeable damage due to fibre breaking along the areas at more significant deformation is evaluated (Fig. 14c). Fig. 14d captures the instant of failure of the specimen with the net failure of the carbon fibres along the section outside the Kevlar window.

Fig. 15 contains various images grabbed with the lateral camera. It is immediately visible that the damage due to delamination manifests externally only in the final phases of the test, highlighted with red circles in Fig. 15d and e. Additionally, a light swelling and bending can be seen, resulting from the presence of the bulge on the back side that causes a loading eccentricity of the central part of the specimen. Overall, it seems that the delamination is spreading out through the section and extends longitudinally until gross failure occurs from the corners of the window in the front side. C-scan investigation to prove this first guess is presented in the next section.

3.3. C-scan damage evolution pattern

Before starting the tests, the specimens were C-scanned to assess their state. Fig. 16a depicts the sample image obtained from the C-scan analysis, where black-red-yellow contours correspond to the presence

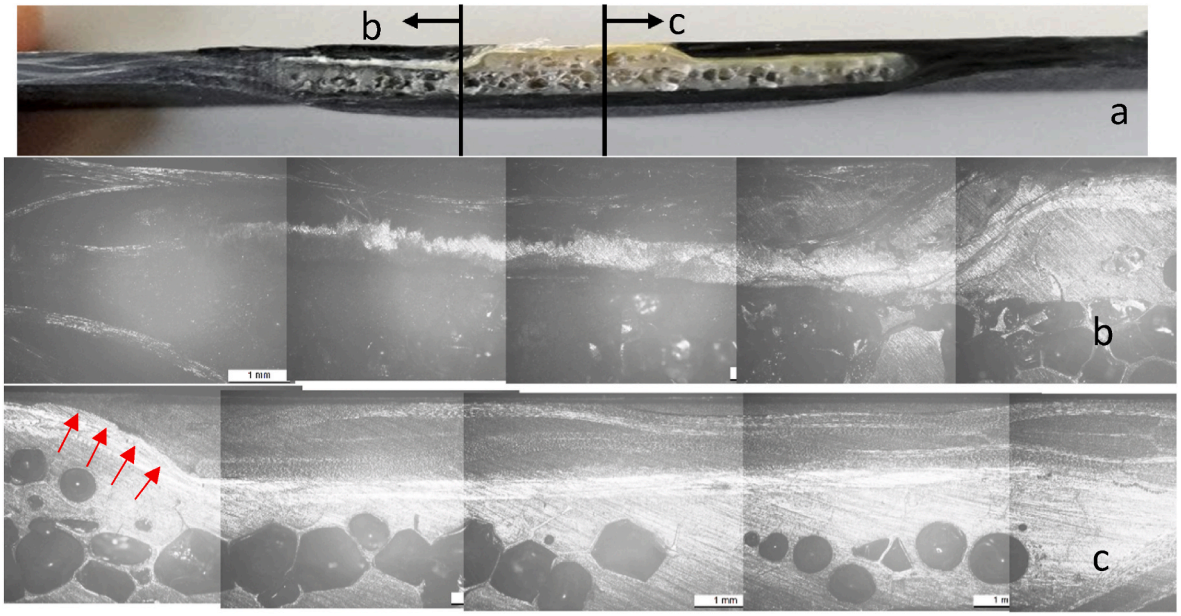

Fig. 18. a) longitudinal section, b) magnification of left side, c) magnification of right side at 44 kN load. Red arrows indicate a crack at the CFRP/Kevlar interface.

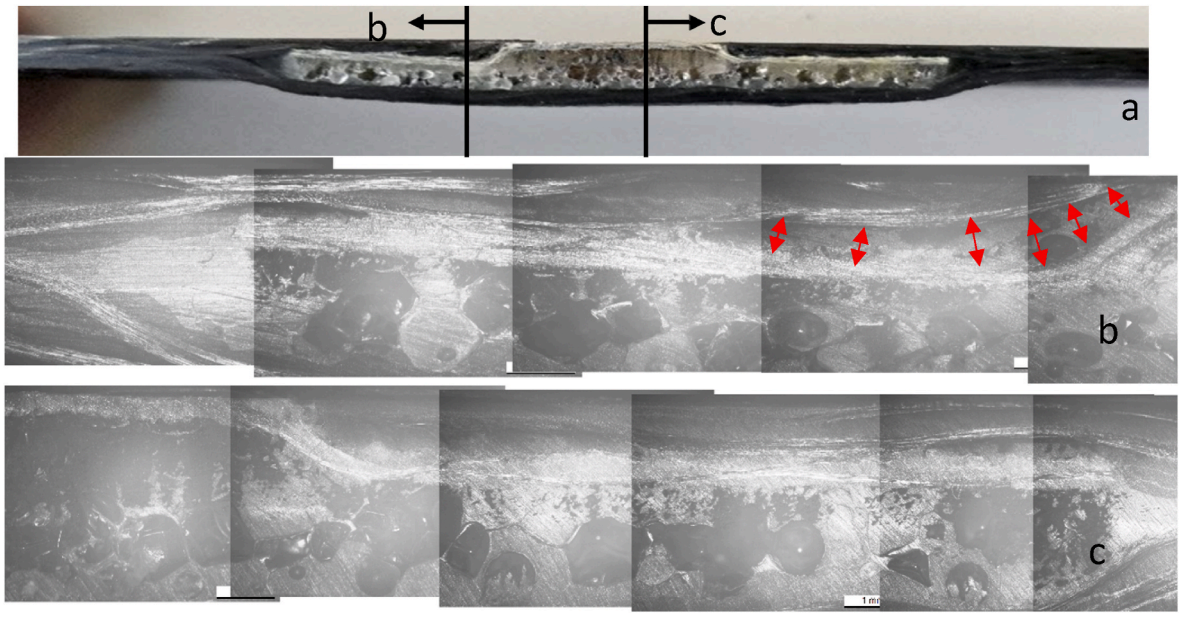

Fig. 19. a) longitudinal section, b) magnification of left side, c) magnification of right side at 50 kN load. Red arrows indicate a crack at the CFRP/Kevlar interface.

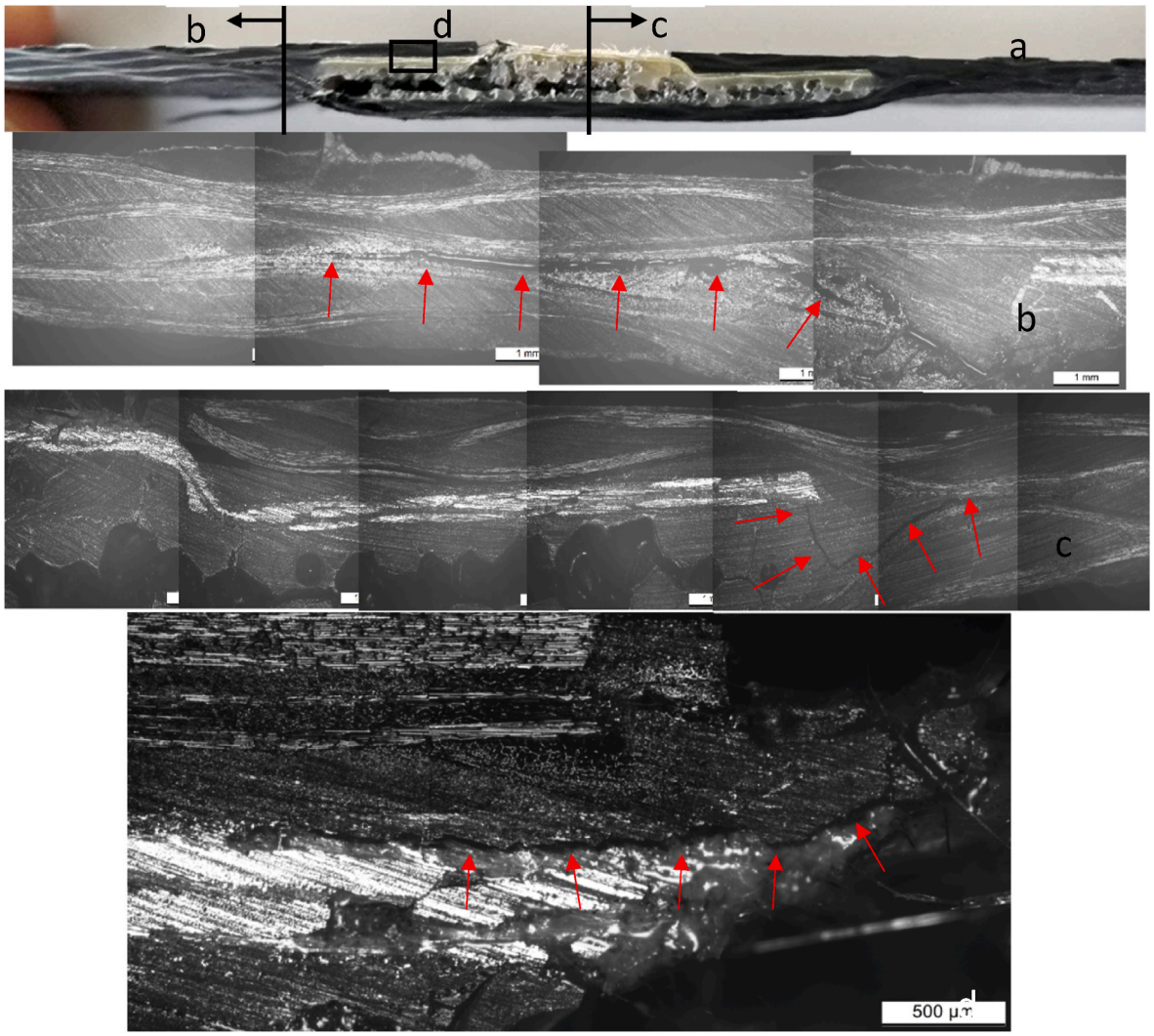

Fig. 20. a) longitudinal section, b) magnification of left side, c) magnification of right side, d) close-up of CFRP/Kevlar interface at failure. Red arrows indicate a crack at the CFRP/Kevlar interface.

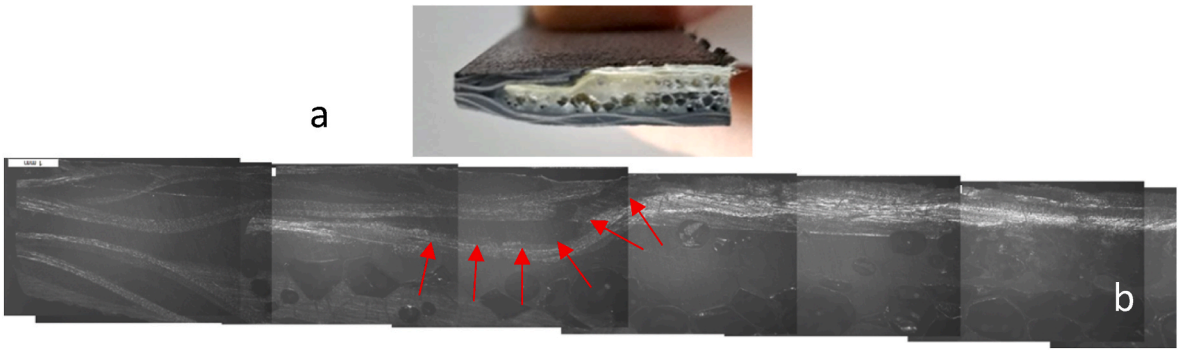

Fig. 21. a) Specimen sectioned along the transverse direction at load, b) optical microscope images at 33 kN load.

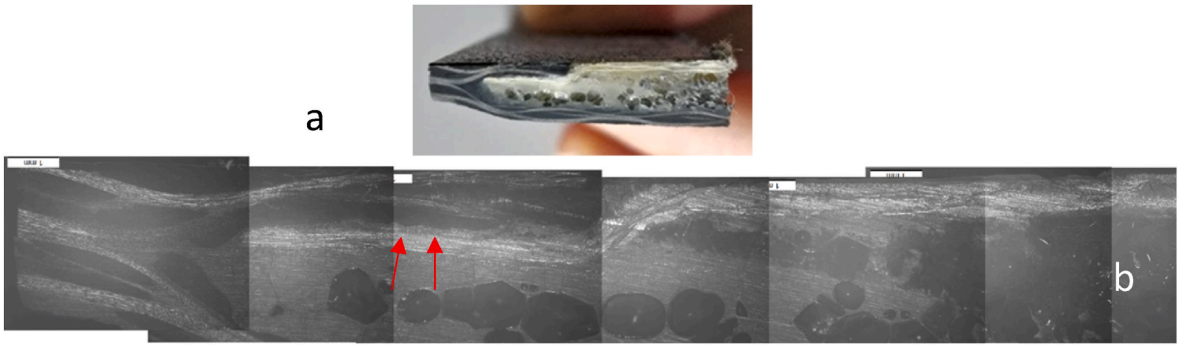

Fig. 22. a) Specimen sectioned along the transverse direction at load, b) optical microscope images at 44 kN load.

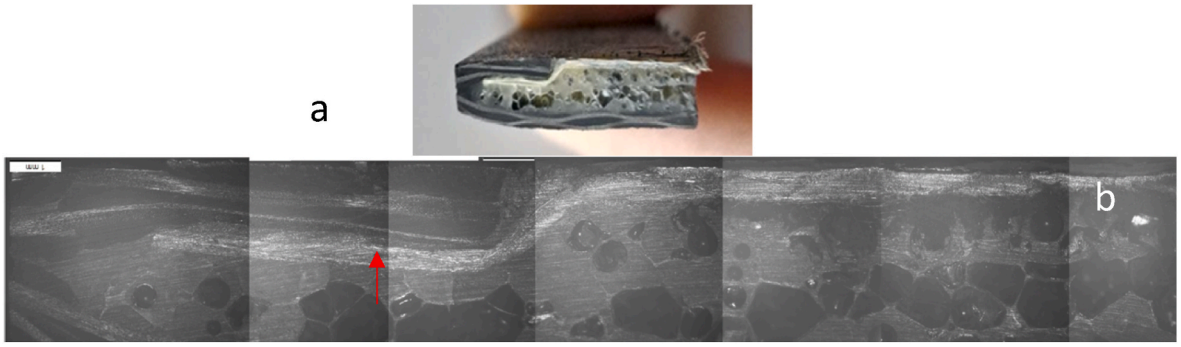

Fig. 23. a) Specimen sectioned along the transverse direction at load, b) optical microscope images at 50 kN load.

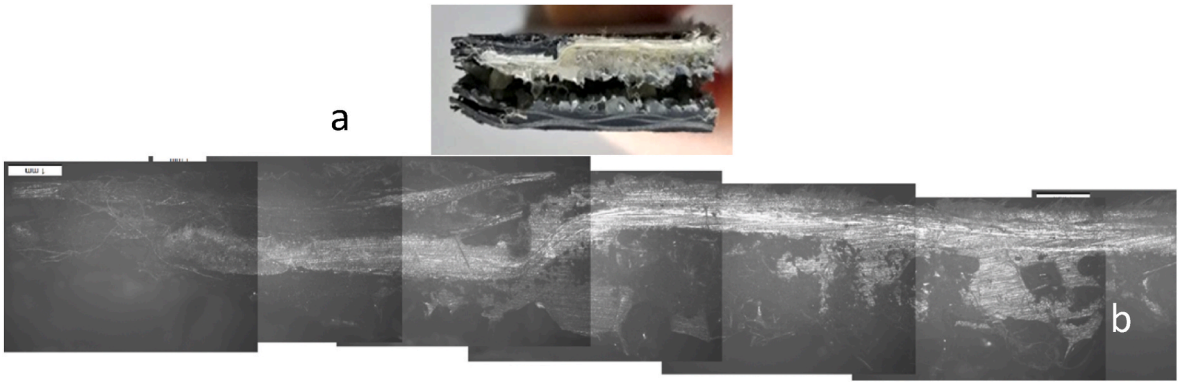

Fig. 24. a) Specimen sectioned along the transverse direction at load, b) optical microscope images at failure load.

Table 5
Summary of recorded AE events.

Specimen	AE Events (tot. counts)	Average Amplitude [dB]	Average Frequency [kHz]
1	180368	80.9	91.95
2	195290	78.6	94.68
3	155207	79.98	96.61
4	120483	80.14	96.64
5	148945	80.42	106.08

Rohacell insert with a hole in the middle to simulate the tag placement and resin meniscus at the periphery.

Fig. 16b show the C-scan of the failed specimen, where the delaminated area expands well above and below the Rohacell insert. The progression of delamination has been studied and reported in the section on interrupted tensile tests.

3.4. OM analysis

Longitudinal sections are reported in Figs. 17–20. At 33 kN, damage cannot be detected under the OM in the longitudinal direction (Fig. 17), while at 44 kN a small crack can be seen at the interface between CFRP and Kevlar (Fig. 18c). A similar situation, but much more pronounced, is seen in Fig. 19b (50 kN). The region indicated by red arrows in Fig. 19b is also a critical point in manufacturing, since a perfect matching of the CFRP plies to the Kevlar insert is very hard to realize.

Fig. 20a represents a failed specimen. In Fig. 20b, a delamination between the front and back plies of CFRPs is visible, that is in agreement with the C-scan of Fig. 16. In Fig. 20c, on the other hand, a crack is seen to start at the end of the Kevlar insert and runs into the matrix pocket until it reaches the CFRP plies, where it transforms into a delamination crack. Finally, Fig. 20d shows the debonding of the CFRP/Kevlar in the window region, alike in Figs. 18c and 19b.

Transverse sections are reported in Figs. 21–24. At 33 kN (Fig. 21), a detachment is visible between CFRP from Kevlar in the window region, that confirms how damage in this region starts quite early. A similar situation, though less pronounced, is seen in Fig. 22b (44 kN) and Fig. 23b (50 kN). However, the section of a failed specimen (Fig. 24) highlights that the finally prevailing failure mode is delamination of the CFRP plies, beside of course fibre failure as shown in Fig. 14.

3.5. AE analysis

The values extracted from the AEs as total counts, average Amplitude and average Peak Frequency (PF) for the respective tests are reported in Table 5. When comparing the values obtained, it can be seen that the average amplitude and PF values obtained are similar among the specimens, meaning that the damage mechanisms is the same in all specimens.

In order to better understand the data obtained from the tests, graphs of AE events as a function of force, normalised to the force at failure, are shown in Fig. 25. For the sake of simplicity, since the response of the specimens was very similar to each other, only one specimen will be illustrated.

Fig. 25 highlights the dispersion of the raw data obtained from the reference test as a function of amplitude Fig. 25a and the distribution as a function of peak frequency in Fig. 25b. It is evident that events of higher amplitude and frequency occur after 50–60 % of the failure load, that is around 30 kN. This is consistent with Fig. 13, where visible force drops occur above 40 kN.

The AE data were then clustered according to the procedure described previously. In Fig. 26, the clustering of the AE events in terms of amplitude per cluster is shown as a function of test time, together with the accumulated energy per cluster and the force. Therefore, in order to discard background noise, the morphology of the waveform of each cluster was analysed and shown in Fig. 27, where it can be seen that cluster number 1 has a continuous waveform type and can be therefore associated, at least partly, to a background noise.

An additional step of filtering has been carried out by recording AE of a virgin specimen at zero load for approximately 500 s. The portion of

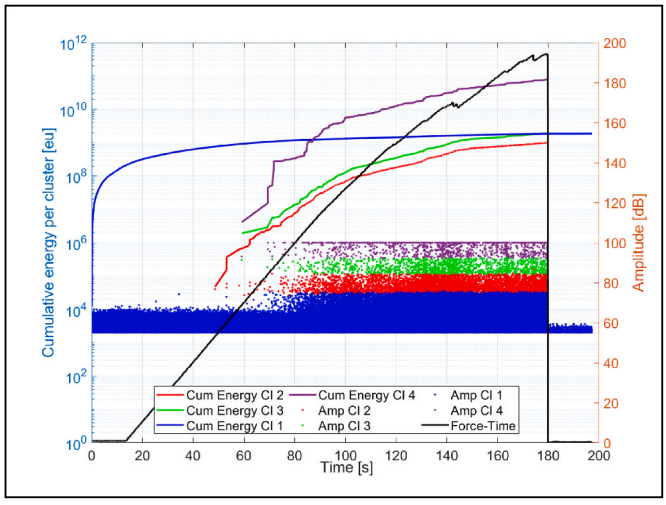

Fig. 26. AE event groups for each cluster (before filtering for background noise).

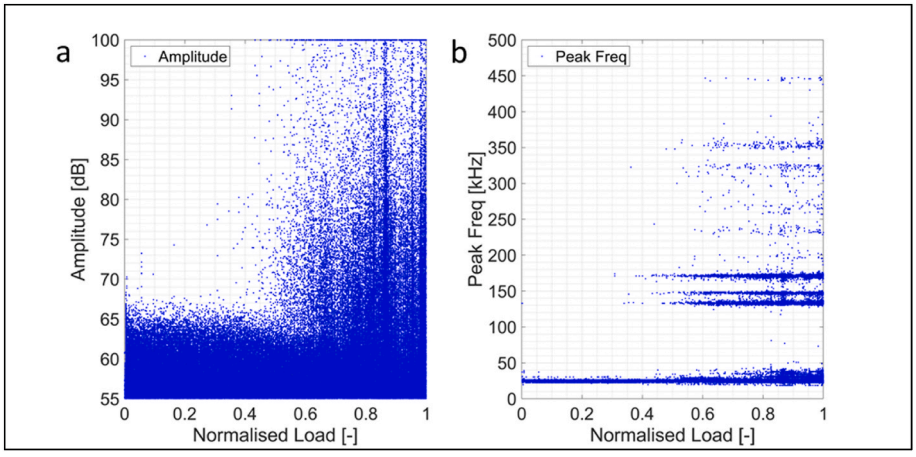

Fig. 25. Events of AE vs Normalised load a) Amplitude, b) Peak Frequency during the tensile test of the specimen number 1.

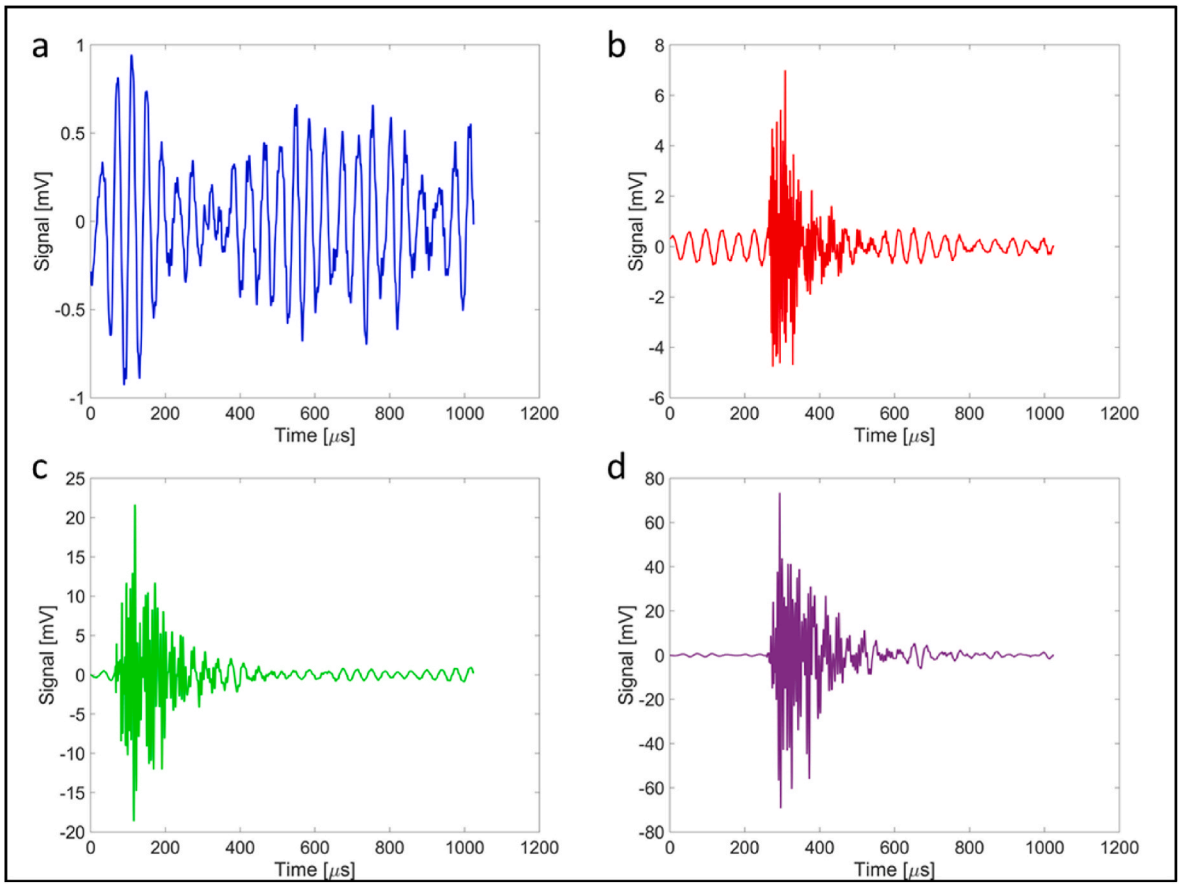

Fig. 27. Representative waveforms of each cluster a) Cluster 1, b) Cluster 2, c) Cluster 3, d) Cluster 4.

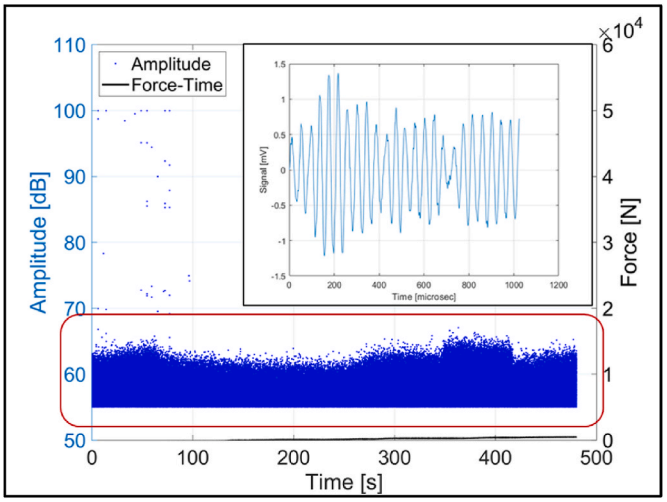

Fig. 28. AE events under zero loading with a representative waveform of the domain.

signal below 65 dB of amplitude contains continuous waves, shown in Fig. 28, that can be related to noise from the testing machine. So as in Refs. [30,31] it was decided to remove all events below 65 dB from the AE dataset.

The application of this filter reduced greatly the number of events analysed, being the hits after filtering just 10–20 % of those before (see Table 5) depending on the specimen. In Table 6, the total count and those pertaining to the single clusters are reported, that highlights a prevalence in counts of Cluster 1. Nevertheless, after filtering the

Table 6
Data analysed after filtering of the hits below 65 dB of amplitude.

Specimen	Counts after filtering	Cluster 1	Cluster 2	Cluster 3	Cluster 4
1	24770	13334	7840	2105	1491
	%	53.83	31.65	8.50	6.02
2	20459	10963	5874	1875	1747
	%	53.59	28.71	9.16	8.54
3	28263	14210	9162	2776	2115
	%	50.28	32.42	9.82	7.48
4	14054	7132	4049	1461	1412
	%	50.75	28.81	10.40	10.05
5	29952	15346	9495	2889	2222
	%	51.24	31.70	9.65	7.42

waveform associated to this Cluster is of the burst type (Fig. 29), so it can be related to some form of damage, too.

The diagram of Fig. 26 has been reproduced in Fig. 30 after filtering, and now events in all four clusters start at a force of 20–25 kN, with just a few hits in Cluster 1 below that value, that may be residual noise.

Considering the amplitude intervals of the different clusters shown in Fig. 30, the first cluster can be associated with matrix cracking since it is within the 65–72 dB amplitude range [18]. As noted by Ref. [32] while increasing load, cracks arise at the longitudinal and transverse fiber/-matrix interface with amplitudes in the 72–82 dB range (Cluster 2). With the increase in load also fibers begin to break. The fiber break is typically in the range 82–92 dB [18,32] of cluster 3. The Cluster 4 with the highest energy release and amplitude, is related to a delamination phenomenon (92–100 dB) [17,33]. By the way, the duration and the rise time of the AE signal bursts of cluster four are longer than that of cluster three (avg. duration 3371 against 1425 μs; avg. rise time 596 against 396 μs), which

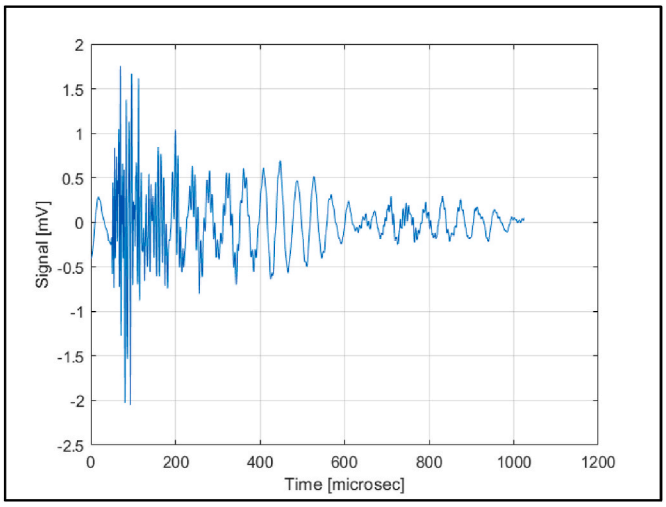

Fig. 29. Representative waveforms of cluster one after filtering the noise.

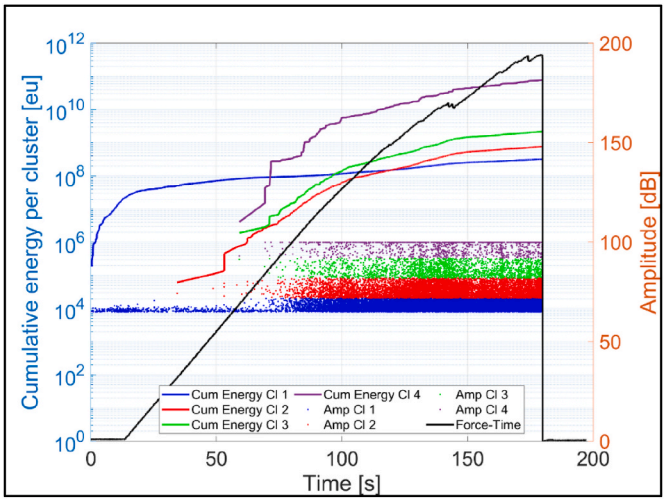

Fig. 30. AE event groups for each cluster (after filtering for background noise).

is consistent with Dzenis et al. [23], that suggests damage due to delamination has a longer duration than fibre failure, and with [24], that claims the rise time in fiber failure is lower than that of delamination.

In synthesis, AE gives us the information that all the failure mechanisms (matrix cracking, fiber-matrix detachment, fibre failure and delamination) are simultaneously active above 50 % of the maximum force. The beginning of damage above 50 % of the maximum load is also coherent with the fact that a bulk, plain specimen made of CFRP would have had a failure load that is twice the one recorded in these experiments. The simultaneous development is justified by the complex geometry of the specimen, where matrix cracking and delamination start around the window in the CFRP on the front side of the specimen, as seen by DIC, then delamination involves the Rohacell insert and the interface between the upper and lower CFRP plies and it finally runs across the whole section, as testified by the C-scan images. Fiber breakage initiates soon from corners of the window in the CFRP on the front side, too, leading to the final catastrophic failure.

3.6. *Interrupted tensile tests*

The purpose of these tests was to monitor the evolution of damage by C-scan and by OM. DIC and AE were used, too, and their results just confirmed what was recorded in non-interrupted tensile tests. The entire test was initially divided into five intervals, i.e. every 11 kN according to the average maximum load found in the quasi-static tests; the last ramp led to specimen breaking. However, when analysing C-scan images, it was noticed that delamination progressed largely in the instants before failure. Therefore, it was decided to add a further interval up to 50 kN, i.e., just before the specimen breaks. For the sake of simplicity, the results obtained from one specimen will be shown, but the results of the others are overlapping.

3.7. *C-scan damage evolution pattern*

The evolution of the delamination as detected by C-scan is shown in Fig. 31. The red and black area at zero load correponds to the Rohacell insert with the cavity for the tag. Subsequently, as each load step is reached, a progressive debonding of the insert occurs. Upon reaching 44 kN, the debonding reaches the edges of the insert. At 50 kN, the delamination starts to affect the carbon plies with some small cracks on the edge of the specimen, corresponding to a series of small drops in the force-time curve and, consequently, jumps in the cumulative energy and cumulative counts of the AE signal can be seen.

4. Conclusions

The influence of the integration of a RFID tag inside a CFRP laminate was examined with respect the quasi-static strength and the failure mode, using both destructive and non-destructive techniques. The main conclusions are as follows:

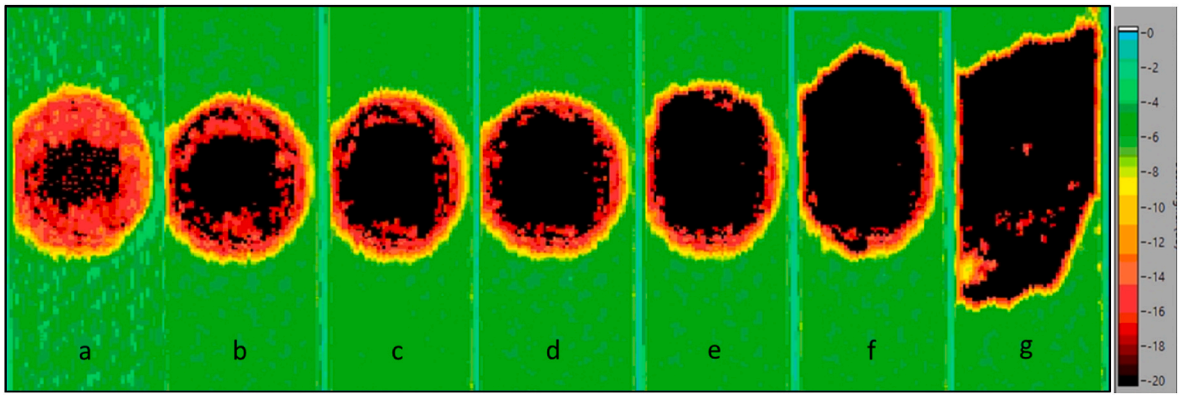

Fig. 31. Pictures given back from C-scan of the force levels: a)0 kN, b)11 kN, c)22 kN, d)33 kN, e)44 kN, f)50 kN, g)after failure load. The scale represents the attenuation of ultrasound wave in dB.

- The quasi-static strength is about half of that expected by a plain laminate composed by the same CFRP plies. A reinforcement has therefore to be devised to recover the expected strength as much as possible;
- the DIC and the OM indicated that the connection between CFRP and the Kevlar insert in the region around the CFRP window on the front side, is prone to an early debonding. Even though this is not the main cause of failure under quasi-static loading, it may become a starting point for a fatigue crack;
- final failure occurs in the CFRP front plies at the corners of the "window" created to house the Kevlar insert, due to strong stress concentration. Since Kevlar is necessary to allow electromagnetic waves to go back and forth from the RFID tag, a better continuity with CFRP should be studied to lower the stress concentration, rethinking the manufacturing cycle;
- the C-scan of interrupted tests showed that damage is confined within the bulge region of the specimen until it is close to failure, where delamination spreads over the borders of the bulge. The OM further revealed that it occurred between the CFRP and Kevlar insert and between the front and back CFRP plies;
- the AE signal was analysed using an ANN-SOM algorithm, which resulted four different clusters in terms of amplitude of the events. Based on literature, these clusters of events should correspond to matrix cracking, fibre/matrix interface debonding, delamination and fibre failure. Since in the four clusters are overlapped in time, the four failure mechanisms are active contemporarily.

CRediT authorship contribution statement

Daniele Ambrosini: Conceptualization, Data curation, Investigation. **Dimitrios Zarouchas:** Methodology, Supervision. **Alessandro Pirondi:** Conceptualization, Supervision, Writing – original draft, Writing – review & editing. **Luca Vescovi:** Resources, Supervision.

Declaration of competing interest

The authors declare that they have no known competing financial interests or personal relationships that could have appeared to influence the work reported in this paper.

Data availability

Data will be made available on request.

References

[1] J.V. da Rocha Pasqualeto, V.T. Gomes Costa, Industry 4.0 and RFID in the automotive sector: a case study on the implementation of RFID technology in automaker's supply, Journal of Automation 1 (2) (2018) 78–92.

[2] C. Occhiuzzi, S. Amendola, S. Nappi, N. D'Uva, G. Marrocco, RFID technology for industry 4.0: Architectures and Challenges, in: IEEE International Conference on RFID Technology and Applications (RFID-TA), 25-27 September 2019, pp. 181–186. Pisa, Italy.

[3] C. Gorldt, D. Uckelmann, U. Hinrichs, J.T. Tervo, Tracking and tracing in production Scenarios with passive RFID Transponders, in: 3rd European Workshop on RFID Systems and Technologies, Duisburg, Germany, 2007, pp. 1–6.

[4] G. Marrocco, C. Occhiuzzi, F. Amato, Sensor-oriented passive RFID, in: The Internet of Things, Proceedings of the 20th Tyrrenian Workshop on Digital Communication, September 2009, pp. 273–282. Pula, Italy.

[5] S.A. Weis, RFID (Radio frequency identification): Principles and application, System 2 (3) (2007) 1–23.

[6] M. Strassner, E. Fleisch, M-lab - the Promise of Auto-ID in the Automotive Industry, MIT Auto-ID Center, Cambridge, MA, USA, 2003.

[7] T.R. Philipp, G. Reinhart, Evaluation of RFID technology application in production of fiber-reinforced Plastics, in: H. El Maraghy (Ed.), Enabling Manufacturing Competitiveness and Economic Sustainability, Springer, Berlin, 2012, pp. 263–268.

[8] M. Brink, F. Berkemeyer, J.-H. Ohlendorf, G. Dumstorff, K.-D. Thoben, W. Lang, Challenges and opportunities of RFID Sensortags integration by fibre-reinforced Plastic components production, Procedia Manuf. 24 (2018) 54–59.

[9] P. Górski, J. Lewandowski, P. Krowicki, T. Lewandowski, Analysis of composite structure effect on Radio-frequency characteristics of the RFID tag, in: E. Rusiński, D. Pietrusiak (Eds.), Proceedings of the 14th International Scientific Conference: Computer Aided Engineering. CAE 2018. Lecture Notes in Mechanical Engineering, Springer, Cham., 2019, pp. 242–251.

[10] J. Pielmeier, G. Reinhart, Rfid integration as an application to industrialize and qualify high-volume composite production, in: International EURASIP Workshop on RFID Technology (EURFID), Rosenheim, Germany, 2015, pp. 157–161.

[11] D. Ambrosini, A. Pirondi, L. Vescovi, F. Arbucci, F. Gabba, Feasibility study for the implementation of RFID technology in CFRPs component, in: 2021 IEEE International Conference on Omni-Layer Intelligent Systems (COINS), 2021, pp. 1–6. Barcelona, Spain.

[12] D. Ambrosini, A. Pirondi, L. Vescovi, F. Arbucci, Performance evaluation of a UHF passive RFID tag embedded in a carbon fibre-reinforced polymer, Int. J. Real. Ther. 13 (1) (2023) 37–51.

[13] X. Li, Nanoscale structural and mechanical characterization of natural nanocomposites: seashells, JOM 59 (3) (2007) 71–74.

[14] X. Li, H. Gao, W.A. Scrivens, D. Fei, V. Thakur, M.A. Sutton, A.P. Reynolds, M. L. Myrick, Structural and mechanical characterization of nanoclay-reinforced agarose nanocomposites, Nanotechnology 16 (10) (2005 Oct) 2020–2029.

[15] N. Song, Z. Gao, X. Li, Tailoring nanocomposite interfaces with graphene to achieve high strength and toughness, Sci. Adv. 6 (2020) eaba7016.

[16] R.K. Heslehurst, Defects and Damage in Composite Materials and Structures, CRC press, Boca Raton, FL, USA, 2014.

[17] P. Nimdum, J. Renard, Use of acoustic emission to discriminate damage modes in carbon fibre reinforced epoxy laminate during tensile and buckling loading, in: ECCM 15 - 15th European Conference on Composite Materials, 24-28 June 2012, p. 8. Venice.

[18] M. Babu, T. Prakash, Characterisation of fiber failure mode in T–700 carbon fiber reinforced epoxy, Russ. J. Nondestr. Test. 50 (2014) 45–57.

[19] R. Gutkin, C. Green, S. Vangrattanachai, S. Pinho, P. Robinson, P. Curtis, On acoustic emission for failure investigation in CFRP: pattern recognition and peak frequency analyses, Mech. Syst. Signal Process. 25 (2011) 1393–1407.

[20] N. Godin, S. Huguet, R. Gaertner, Integration of the Kohonen's self-organising map and k-means algorithm for the segmentation of the AE data collected during tensile tests on cross-ply composites, NDT E Int. 34 (4) (2005) 299–309.

[21] P.J. de Groot, P.A.M. Wijnen, R.B.F. Janssen, Real-time frequency determination of acoustic emission for different fracture mechanisms in carbon/epoxy composites, Compos. Sci. Technol. 55 (4) (1995) 405–412.

[22] C.R. Ramirez-Jimenez, N. Papadakis, N. Reynolds, T.H. Gan, P. Purnell, M. Pharaoh, Identification of failure modes in glass/polypropylene composites by means the primary frequency content of the AE event, Compos. Sci. Technol. 60 (2004) 1819–1827.

[23] Y.A. Dzenis, J. Qian, Analysis of microdamage evolution histories in composites, Int. J. Solid Struct. 38 (10–13) (2001) 1831–1854.

[24] P. Ding, Q. Li, X. Huang, Classification of acoustic emission sources produced by carbon/epoxy composite based on support vector machine, IOP Conf. Ser. Mater. Sci. Eng. 87 (2015) 012002.

[25] R.A.A. Lima, M. Drobiazko, A. Bernasconi, M. Carboni, On crack tip localisation in quasi-statically loaded, adhesively bonded double cantilever beam specimens by acoustic emission, Theor. Appl. Fract. Mech. 118 (2022) 103286.

[26] D. Crivelli, M. Guagliano, A. Monici, Development of an artificial neural network processing technique for the analysis of damage evolution in pultruded composites with acoustic emission, Compos. B Eng. (56) (2014) 948–959.

[27] P.J. Rousseeuw, Silhouettes: a graphical aid to the interpretation and validation, Comput. Appl. Math. 20 (1987) 53–65.

[28] D.L. Davies, D.W. Bouldin, A cluster separation measure, IEEE Trans. Pattern Anal. Mach. Intell. 1 (2) (1979) 224–227.

[29] T. Calinski, J. Harabasz, A dendrite method for cluster analysis, Commun. Stat. 3 (1974) 1–27.

[30] J.A. Pascoe, D.S. Zarouchas, R.C. Alderliesten, R. Benedictus, Using acoustic emission to understand fatigue crack growth within a single load cycle, Eng. Fract. Mech. 194 (2018) 281–300.

[31] M. Fotouhi, P. Suwarta, M. Jalalvand, G. Czel, M.R. Wisnom, Detection of fibre fracture and ply fragmentation in thin-ply UD carbon/glass hybrid laminates using acoustic emission Composites Part A, Applied Science and Manufacturing 86 (2016) 66–76.

[32] P.F. Liu, J.K. Chu, Y.L. Liu, J.Y. Zheng, A study on the failure mechanisms of carbon fiber/epoxy composite laminates using acoustic emission, Mater. Des. 37 (2012) 228–235.

[33] H.Y. Chou, A.P. Mouritz, M.K. Bannister, A.R. Bunsell, Acoustic emission analysis of composite pressure vessels under constant and cyclic pressure, Compos. Appl. Sci. Manuf. 70 (2015) 111–120.